

KMT-2016-BLG-1337L: A Saturn-mass planet orbiting within a binary system of low-mass stars

CHEONGHO HAN,¹ CHUNG-UK LEE,² IAN A. BOND³ AND ANDRZEJ UDALSKI⁴

(LEADING AUTHORS)

MICHAEL D. ALBROW,⁵ SUN-JU CHUNG,² ANDREW GOULD,⁶ YOUN KIL JUNG,^{2,7} KYU-HA HWANG,² YOON-HYUN RYU,² YOSSI SHVARTZVALD,⁸ IN-GU SHIN,⁹ JENNIFER C. YEE,¹⁰ WEICHENG ZANG,⁹ HONGJING YANG,⁹ DOEON KIM,¹ DONG-JIN KIM,² SANG-MOK CHA,^{2,11} SEUNG-LEE KIM,² DONG-JOO LEE,² YONGSEOK LEE,^{2,11} BYEONG-GON PARK² AND RICHARD W. POGGE⁶

(KMTNET COLLABORATION)

FUMIO ABE,¹² DAVID P. BENNETT,^{13,14} APARNA BHATTACHARYA,^{13,14} RYUSEI HAMADA,¹⁵ YUKI HIRAO,¹⁶ ASAHI IDEI,¹⁵ STELA ISHITANI SILVA,¹³ SHOTA MIYAZAKI,¹⁵ YASUSHI MURAKI,¹⁷ TUTUMI NAGAI,¹⁵ KANSUKE NUNOTA,¹⁵ GREG OLMSCHENK,¹³ CLÉMENT RANC,¹⁸ NICHOLAS J. RATTENBURY,¹⁹ YUKI SATOH,¹⁵ TAKAHIRO SUMI,¹⁵ DAIKUKE SUZUKI,¹⁵ TAKUTO TAMAOKI,¹⁵ SEAN K. TERRY,^{13,14} PAUL J. TRISTRAM,²⁰ AIKATERINI VANDOROU^{13,14} AND HIBIKI YAMA¹⁵

(MOA COLLABORATION)

PRZEMEK MRÓZ,⁴ MICHAŁ K. SZYMAŃSKI,⁴ JAN SKOWRON,⁴ RADOSŁAW POLESKI,⁴ IGOR SOSZYŃSKI,⁴ PAWEŁ PIETRUKOWICZ,⁴ SZYMON KOZŁOWSKI,⁴ KRZYSZTOF A. RYBICKI,^{4,8} PATRYK IWANEK,⁴ KRZYSZTOF ULACZYK,²¹ MARCIN WRONA,^{4,22} MARIUSZ GROMADZKI⁴ AND MATEUSZ J. MRÓZ⁴

(THE OGLE COLLABORATION)

¹ Department of Physics, Chungbuk National University, Cheongju 28644, Republic of Korea

² Korea Astronomy and Space Science Institute, Daejon 34055, Republic of Korea

³ Institute of Natural and Mathematical Science, Massey University, Auckland 0745, New Zealand

⁴ Astronomical Observatory, University of Warsaw, Al. Ujazdowskie 4, 00-478 Warszawa, Poland

⁵ University of Canterbury, Department of Physics and Astronomy, Private Bag 4800, Christchurch 8020, New Zealand

⁶ Department of Astronomy, Ohio State University, 140 West 18th Ave., Columbus, OH 43210, USA

⁷ University of Science and Technology, Daejeon 34113, Republic of Korea

⁸ Department of Particle Physics and Astrophysics, Weizmann Institute of Science, Rehovot 76100, Israel

⁹ Department of Astronomy, Westlake University, Hangzhou 310030, Zhejiang Province, China

¹⁰ Center for Astrophysics | Harvard & Smithsonian 60 Garden St., Cambridge, MA 02138, USA

¹¹ School of Space Research, Kyung Hee University, Yongin, Gyeonggi 17104, Republic of Korea

¹² Institute for Space-Earth Environmental Research, Nagoya University, Nagoya 464-8601, Japan

¹³ Code 667, NASA Goddard Space Flight Center, Greenbelt, MD 20771, USA

¹⁴ Department of Astronomy, University of Maryland, College Park, MD 20742, USA

¹⁵ Department of Earth and Space Science, Graduate School of Science, Osaka University, Toyonaka, Osaka 560-0043, Japan

¹⁶ Institute of Astronomy, Graduate School of Science, The University of Tokyo, 2-21-1 Osawa, Mitaka, Tokyo 181-0015, Japan

¹⁷ Institute for Space-Earth Environmental Research, Nagoya University, Nagoya 464-8601, Japan

¹⁸ Sorbonne Université, CNRS, UMR 7095, Institut d'Astrophysique de Paris, 98 bis bd Arago, 75014 Paris, France

¹⁹ Department of Physics, University of Auckland, Private Bag 92019, Auckland, New Zealand

²⁰ University of Canterbury Mt. John Observatory, P.O. Box 56, Lake Tekapo 8770, New Zealand

²¹ Department of Physics, University of Warwick, Gibbet Hill Road, Coventry, CV4 7AL, UK

²² Villanova University, Department of Astrophysics and Planetary Sciences, 800 Lancaster Ave., Villanova, PA 19085, USA

ABSTRACT

We report the discovery and characterization of a planetary companion in the microlensing event KMT-2016-BLG-1337, which was produced by a binary system of low-mass stars. The light curve of the event exhibits a short-term anomaly superposed on the profile of a binary-lens single-source (2L1S) model. To investigate the nature of this anomaly, we performed detailed modeling under both the

binary-lens binary-source (2L2S) and triple-lens single-source (3L1S) interpretations. The 3L1S model provides a substantially better fit to the data, strongly favoring the presence of a planetary companion in the lens system. Two viable 3L1S solutions describe the event nearly equally well. In one solution, the planet has a mass of $M_3 \sim 0.3 M_J$ and lies at a projected separation of $a_{\perp,3} \sim 4$ au from the heavier member of the host binary. In the alternative solution, the planet has a mass of $M_3 \sim 7 M_J$ and a projected separation of $a_{\perp,3} \sim 1.5$ au. The host binary consists of early M-type dwarfs with masses of $M_1 \sim 0.54 M_{\odot}$ and $M_2 \sim 0.40 M_{\odot}$, separated in projection by $a_{\perp,2} \sim 3.5$ au. The system is located at a distance of $D_L \sim 7$ kpc toward the Galactic bulge. This event demonstrates the sensitivity of microlensing to planets in dynamically complex stellar environments, including systems beyond the reach of other detection techniques. It thereby contributes to a more comprehensive understanding of planet formation in multiple-star systems.

Keywords: Gravitational microlensing (672) – exoplanet detection (2147)

1. INTRODUCTION

Detecting planets in binary star systems is crucial for deepening our understanding of how planets form and evolve. Traditional planet formation theories were developed primarily for single-star systems, like our Solar System, but binary systems introduce additional gravitational complexities that can disrupt or reshape protoplanetary disks. The discovery of planets within these systems challenges classical assumptions and demonstrates that planet formation is more resilient and adaptable than once believed. Such findings help refine theoretical models such as core accretion and disk instability, leading to a more comprehensive view of planetary origins.

The study of planets in binaries also holds significant statistical importance. Since roughly half of all stars in the Milky Way exist in binary or multiple systems, excluding them would leave our understanding of planetary populations incomplete. By including binary systems in exoplanet surveys, astronomers can develop a more accurate estimate of how common planetary systems are throughout the Galaxy and how stellar multiplicity influences their distribution.

The microlensing technique plays a uniquely powerful role in this field. It can reveal planets found in many types of binary systems, including those that orbit both stars (circumbinary systems), those that orbit only one star in the pair (C. Han et al. 2017a), and those that belong to one star while the other influences the gravitational lensing effect. This flexibility makes microlensing more effective for studying complex systems than most other planet detection methods.

Another key advantage of microlensing is its independence from the light of the host star. Because it relies on gravitational effects rather than direct light detection, microlensing can identify planets around faint or non-luminous stars, such as M-dwarfs or brown dwarfs,

even when the system cannot be resolved by telescopes. Moreover, microlensing allows astronomers to detect planets in distant regions of the Galaxy, far beyond the reach of other detection techniques, helping build a more complete Galactic census of planetary systems.

Microlensing surveys conducted since the early 1990s have led to the discovery of ten planets orbiting within binary systems. The lens system OGLE-2006-BLG-284L consists of two low-mass stars and a gas giant planet with a mass ratio of $q = 1.26 \times 10^{-3}$ to the primary (D. P. Bennett et al. 2020). The event OGLE-2013-BLG-0341 revealed a cold super-Earth orbiting a low-mass star in a binary separated by about 15 au, located beyond the system's snow line (A. Gould et al. 2014). OGLE-2008-BLG-092 was modeled as a triple-lens system comprising two stars and an ice giant similar to Uranus, showing that giant planets can form in dynamically perturbed binaries (R. Poleski et al. 2014). OGLE-2007-BLG-349L marked the first discovery of a circumbinary planet through microlensing, revealing a Saturn-mass planet orbiting both stars in the system (D. P. Bennett et al. 2016). In OGLE-2016-BLG-0613, the lens model involved a super-Jupiter bound to one star in a binary, producing complex caustic patterns from triple-lens interactions (C. Han et al. 2017b). OGLE-2018-BLG-1700 revealed a planet that could be either circumprimary or circumbinary, highlighting the degeneracies in multi-lens modeling (C. Han et al. 2020). In the case of the lensing event KMT-2019-BLG-1715, the lens consists of planet-mass object with $\sim 2.6 M_J$ and binary stars of K and M dwarfs lying in the galactic disk (C. Han et al. 2021). KMT-2020-BLG-0414 is an exceptional case in which an Earth-mass planet resides in a binary composed of an M dwarf and a low-mass brown dwarf (W. Zang et al. 2021a). The event OGLE-2023-BLG-0836 required a triple-mass lens model, identifying a binary system with a plane-

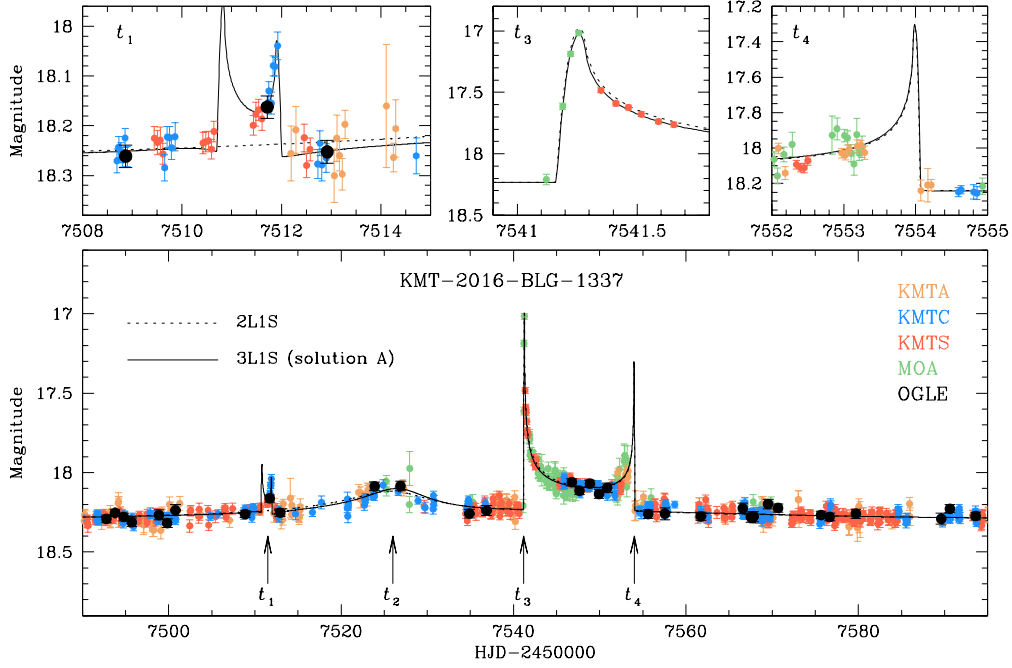


Figure 1. Light curve of the microlensing event KMT-2016-BLG-1337. The lower panel presents the full light curve of the event, with labeled arrows marking the times of the major anomaly features. The upper panels provide enlarged views of the regions around t_1 , t_3 , and t_4 . The dotted and solid curves plotted over the data points represent the model fits for the binary-lens single-source (2L1S) and triple-lens single-source (3L1S: solution A) models, respectively. The colors of the data points correspond to the telescopes used for the observations, as indicated in the legend.

tary companion and marking the sixth such discovery (C. Han et al. 2024). Finally, KMT-2024-BLG-0404L involved a star, brown dwarf, and planet, extending microlensing discoveries to mixed stellar–substellar binaries (C. Han et al. 2025b). Collectively, these detections demonstrate that planet formation and survival are feasible across a wide range of binary configurations, underscoring the resilience and adaptability of planetary systems in diverse dynamical environments.

In this work, we report the discovery of a new microlensing planet residing in a binary stellar system. This planet was identified through a detailed reanalysis of observational data obtained from lensing surveys. The detection adds to the gradually increasing number of microlensing planets found in binary configurations, further illustrating the capability of microlensing to uncover planetary systems that are otherwise difficult to detect. By expanding the sample of known planets in binary systems, this discovery provides an additional data point for testing models of planet formation and stability under the complex gravitational conditions of multiple-star environments.

2. IDENTIFICATION OF PLANETARY SIGNAL

The newly discovered planet was identified through a reanalysis of microlensing events detected by the Ko-

rea Microlensing Telescope Network (KMTNet) survey (S.-L. Kim et al. 2016), which has been in operation since 2015. The primary objective of this reanalysis was to search for subtle planetary signals that may have been missed in previously modeled binary-lens (2L1S) events.

Each year, during the observing season from March to October, the KMTNet survey detects approximately 3,000 microlensing events. The majority of these events are caused by single-lens single-source (1L1S) configurations, for which lensing models are automatically generated in near real-time upon event detection (D.-J. Kim et al. 2018). Planetary signals in these events are initially identified through visual inspection of the resulting light curves. In addition, in order to perform a uniform, objective, and automated search for anomalies across the entire dataset, the KMTNet collaboration employs an automated algorithm. This algorithm, AnomalyFinder (W. Zang et al. 2021b), identifies potential planetary signals by analyzing the residuals between observed data and the best-fit 1L1S microlensing model.

In the case of binary-lens events, short-duration planetary signals can occur when a planetary companion perturbs the magnification pattern produced by the binary-lens system (D.-W. Lee et al. 2008). However, detecting such planetary signals using algorithms like Anoma-

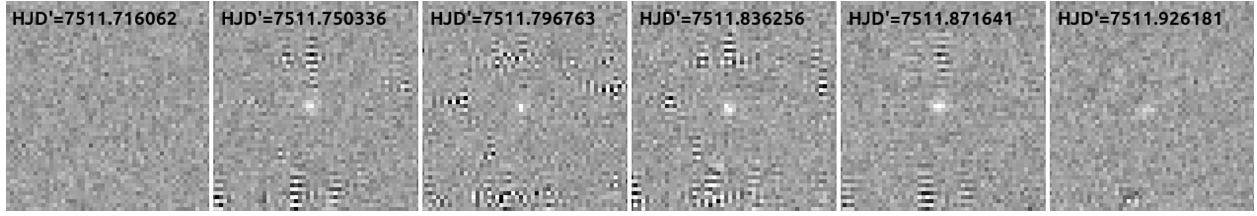


Figure 2. Difference images taken during the planet-induced anomaly around t_1 . The label in each panel indicates the time at which the image was obtained.

lyFinder requires an analysis of the residuals from the binary-lens (2L1S) model. Currently, the modeling of 2L1S events has not yet been fully automated, and therefore, in order to identify planetary signals in these cases, a manual modeling of the 2L1S events must first be conducted. The residuals from these models are then subject to visual inspection to detect possible planetary anomalies. The newly discovered planet orbiting within a binary system, KMT-2016-BLG-1337Lb, was uncovered through a reanalysis of previously detected binary-lens microlensing events from the KMTNet survey.

Figure 1 presents the light curve of the lensing event KMT-2016-BLG-1337, derived from observations obtained by the three KMTNet telescopes and supplemented with data from the Microlensing Observations in Astrophysics (MOA) survey (I. A. Bond et al. 2001; T. Sumi et al. 2003) and the Optical Gravitational Lensing Experiment (OGLE) survey (OGLE; A. Udalski et al. 2015). The light curve displays two distinct spikes at approximately $t_3 \sim 7541.2$ and $t_4 \sim 7554.0$, together with a broad, weak bump centered around $t_2 \sim 7526.0$. This overall pattern is characteristic of a caustic-crossing 2L1S event, in which the two spikes likely correspond to the source's caustic crossings, and the weak bump is probably caused by the source's approach to a cusp of the caustic.

However, a careful inspection of the data revealed a short-term anomaly that could not be explained by the 2L1S model. The anomaly occurred around $t_1 \sim 7511$ and lasted for approximately one day. It shows a characteristic pattern produced by the source's crossing of a tiny caustic, with the second caustic crossing clearly resolved in the data. The anomaly was independently detected in two KMTNet datasets (KMTC and KMTS). In addition, a single data point from the OGLE survey corroborates the anomaly. These independent detections strongly suggest that the anomaly represents a genuine astrophysical signal. This interpretation is further supported by the inspection of the images obtained during the anomaly, as shown in Figure 2. In the following sections, we describe the data acquisition process (Section 3) and provide a detailed analysis of the event (Section 4).

3. OBSERVATIONS AND DATA

The lensing event KMT-2016-BLG-1337 was identified by the KMTNet survey from observations of a source star located toward the Galactic bulge. The equatorial coordinates of the source are (R.A., Decl.) = (17:56:31.21, $-33:02:03.08$), corresponding to the Galactic coordinates (l, b) = ($-2^{\circ}.3340, -4^{\circ}.0998$). The source has a baseline magnitude of $I_{\text{base}} = 18.62$, and the I -band extinction toward the field is $A_I = 1.23$. The event was also independently detected by the MOA survey and designated MOA-BLG-2016-292. Although it was not initially identified by the OGLE survey because of the relatively sparse coverage of this region, OGLE data were subsequently recovered through additional photometric analysis of the source identified by the other surveys. In this paper, we refer to the event using the KMTNet designation.

Observations of the event were conducted using telescopes operated by the three survey groups. The KMTNet survey employs a system of three identical 1.6-meter telescopes, strategically located to provide nearly continuous time coverage of the same sky fields as the Earth rotates. The telescopes are situated at the Cerro Tololo Inter-American Observatory in Chile (KMTC), the South African Astronomical Observatory in South Africa (KMTS), and the Siding Spring Observatory in Australia (KMTA). Each KMTNet telescope is equipped with a mosaic CCD camera composed of four $9k \times 9k$ detectors, offering a wide field of view of approximately 4 square degrees. The MOA survey utilizes a 1.8-meter telescope located at the Mount John University Observatory in New Zealand. Its camera consists of ten $2k \times 4k$ CCDs, providing an effective sky coverage of about 2.2 square degrees. The OGLE survey operates a 1.3-m telescope at Las Campanas Observatory in Chile, equipped with a camera providing a 1.4 square-degree field of view.

The event was observed in the I band by the KMTNet and OGLE surveys and in the customized MOA- R band by the MOA survey. Image reduction and photometric measurements were performed using the respective pipelines developed by M. D. Albrow et al. (2009) for the KMTNet data, A. Udalski (2003) for the

Table 1. Lensing parameters of 2L1S, 2L2S, and 3L1S solutions.

Parameter	2L1S	2L2S	3L1S	
			Solution A	Solution B
χ^2	1719.1	1531.6	1487.5	1490.2
t_0 (HJD')	7538.04 ± 0.12	7540.35 ± 0.40	7537.99 ± 0.44	7538.34 ± 0.40
u_0	0.2703 ± 0.0050	0.2227 ± 0.0050	0.2959 ± 0.0056	0.2989 ± 0.0074
t_E (days)	47.12 ± 0.98	52.33 ± 1.06	41.10 ± 1.10	40.07 ± 1.14
s_2	0.9376 ± 0.0049	0.8884 ± 0.0056	0.9582 ± 0.0041	0.9620 ± 0.0048
q_2	0.658 ± 0.041	0.812 ± 0.050	0.739 ± 0.052	0.819 ± 0.032
α (rad)	2.4675 ± 0.0076	2.5315 ± 0.0200	2.4535 ± 0.0221	2.4647 ± 0.0192
s_3	1.0741 ± 0.0085	0.3939 ± 0.0063
q_3 (10^{-3})	0.49 ± 0.11	12.55 ± 2.34
ψ (rad)	3.591 ± 0.032	0.336 ± 0.020
ρ (10^{-3})	0.962 ± 0.51	0.74 ± 0.04	1.076 ± 0.057	1.082 ± 0.061
$t_{0,2}$ (HJD')	...	7530.33 ± 0.97
$u_{0,2}$...	-0.694 ± 0.016
ρ_2 (10^{-3})
q_F	...	0.222 ± 0.028

NOTE— HJD' \equiv HJD – 2450000.

OGLE survey, and [I. A. Bond et al. \(2001\)](#) for the MOA data. These pipelines employ the difference image analysis technique ([A. B. Tomaney & A. P. S. Croots 1996](#); [R. H. Alard 1998](#); [P. R. Wozniak 2000](#)) to obtain precise photometry in crowded stellar fields. The KMTNet data were subsequently reprocessed using the photometry code developed by [H. Yang et al. \(2025\)](#) to ensure optimal photometric precision.

4. INTERPRETATION OF THE LENSING EVENT

To interpret the anomalous features observed in the lensing light curve, we carried out a series of modeling analyses under various configurations of the lens system. First, considering the presence of caustic spikes in the light curve, we initially modeled the event using a 2L1S configuration. Subsequently, we examined the residuals from the 2L1S model and performed additional modeling to account for anomaly features that could not be explained by this configuration. In this process, we considered both a triple-lens single-source (3L1S) model, which introduces an additional component to the lens system, and a binary-lens binary-source (2L2S) model, in which the source consists of two stars. The results obtained from each model are presented in the following subsections.

4.1. *Binary-lens single-source (2L1S) model*

We began modeling the light curve using the 2L1S configuration. The light curve of a 2L1S event is de-

scribed by seven fundamental parameters. Among these, the first three parameters (t_0, u_0, t_E) characterize the motion of the source relative to the lens. The parameter t_0 denotes the time of the closest approach, u_0 represents the lens-source separation at that time, and t_E indicates the event timescale. Two additional parameters (s, q) define the properties of the binary lens, where s is the projected separation between the two lens components and q is the mass ratio of the components. The parameter α specifies the angle between the source trajectory and the binary lens axis (source incidence angle). Here, both u_0 and s are expressed in units of the angular Einstein radius θ_E . For KMT-2016-BLG-1337, the light curve exhibits distinct caustic crossing features, during which finite source effects become significant. To model these parts accurately, we introduced an additional parameter ρ (normalized source radius), defined as the ratio of the angular source radius θ_* to the angular Einstein radius θ_E .

The modeling was performed to determine the set of lensing parameters, or the lensing solution, that best reproduces the observed light curve. In this procedure, the binary parameters s and q were explored using a grid search, while the remaining parameters were optimized through a downhill minimization method based on the Markov Chain Monte Carlo (MCMC) algorithm. The initial values of the downhill parameters were assigned based on the time of peak, peak magnification, and event

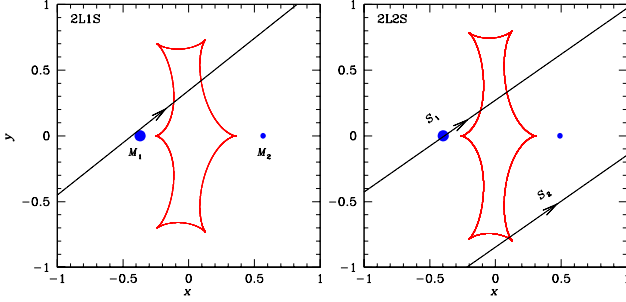


Figure 3. Lens-system configurations of the 2L1S and 2L2S models. In each panel, the two blue dots mark the positions of the binary lens components M_1 and M_2 , where the bigger dot indicates the heavier component. The red closed cuspy curve represents the caustic, and the arrowed line indicates the source trajectory. In the case of the 2L2S model, two source trajectories are shown, one corresponding to the primary source S_1 and the other to the secondary source S_2 . The origin of the coordinate system is set at the barycenter of the lens, and spatial scales are given in units of the angular Einstein radius associated with the combined mass of the lens.

duration. For the source trajectory angle, multiple initial values were evenly distributed within the range of $(0, 2\pi)$.

From the 2L1S modeling, we identified a solution that describes the overall pattern of the light curve. The best-fit binary parameters are $(s, q) \sim (0.94, 0.66)$, with an event timescale of $t_E \sim 47$ days. The complete set of lensing parameters and their uncertainties are listed in Table 1. The model curve corresponding to this best-fit solution is shown as a dotted curve overlaid on the observational data points in Figure 1. The lens system configuration, showing the source trajectory relative to the lens and caustic, is presented in the left panel of Figure 3. It shows that the binary lens forms a resonant caustic due to the binary separation being close to unity, and the source trajectory passes diagonally through the upper region of the caustic. According to this solution, the weak feature observed around t_2 arises from the source's approach to the left on-axis cusp of the caustic, while the two subsequent spikes at t_3 and t_4 are produced as the source crosses the caustic folds. However, the model fails to explain the short-term anomaly at around t_1 .

4.2. Binary-lens binary-source (2L2S) model

An additional short-term anomaly observed in the light curve of a binary-lens event can occur when the source itself is a binary system, as demonstrated by the event KMT-2019-BLG-1715 (C. Han et al. 2021). To explore this possibility, we performed a 2L2S modeling analysis to determine whether the anomaly observed at

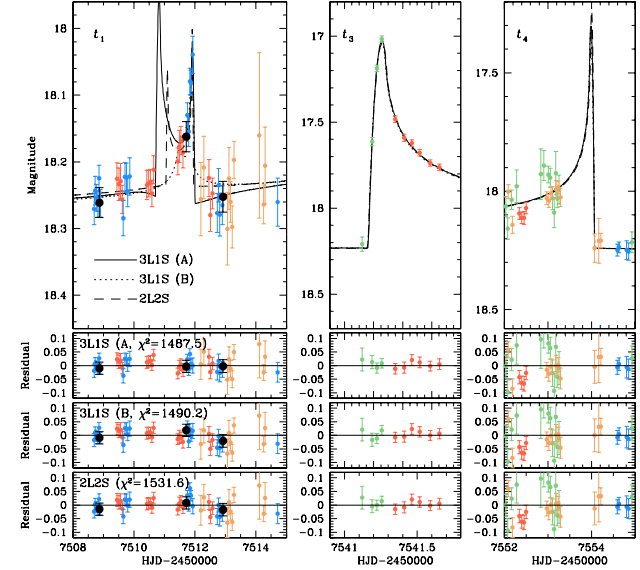


Figure 4. Comparison of the two 3L1S models (solutions A and B) and the 2L2S model in the regions encompassing the three major anomalies around t_1 , t_3 , and t_4 .

t_1 , which could not be explained by the 2L1S model, might originate from a faint companion to the source.

The 2L2S configuration corresponds to the case in which an additional source star is included compared to the 2L1S configuration. Consequently, 2L2S modeling requires additional parameters to describe the secondary source star (S_2). These parameters are $(t_{0,2}, u_{0,2}, \rho_2, q_F)$, where the first two denote the time and separation at the closest approach, the third represents the normalized source radius of S_2 , and the last (q_F) is the flux ratio between the secondary and primary source star (S_1). Because the 2L1S model adequately explains the overall light curve, including the three anomaly features at t_2 , t_3 , and t_4 , the 2L2S modeling was performed with a focus on identifying a secondary source trajectory that could account for the additional anomaly observed at t_1 .

In Table 1, we present the lensing parameters of the best-fit 2L2S solution. A zoomed-in view of the model light curve in the regions around the major anomalies is shown in Figure 4, where the model curve (dashed line) is overlaid on the data points. The model reproduces the anomaly near t_1 , as well as those around the other anomaly features, reasonably well. The right panel of Figure 3 illustrates the corresponding lens configuration, indicating that the anomaly at t_1 arises from the secondary source passing over the tip of the lower-right caustic cusp. The secondary source is considerably fainter than the primary, with a flux ratio of $q_F \sim 0.22$.

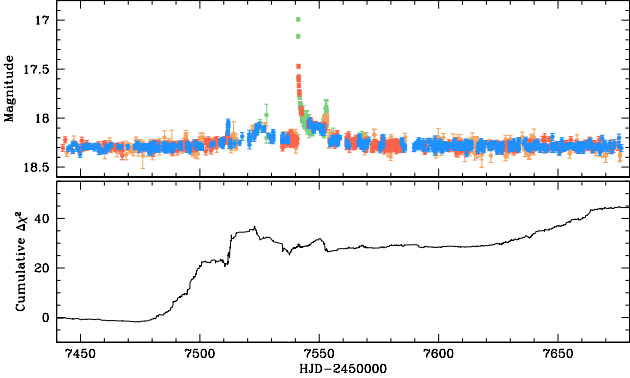


Figure 5. Cumulative distribution of χ^2 difference between the 2L2S and 3L1S model. The light curve in the upper panel is presented to show the region of χ^2 difference.

4.3. Triple-lens single-source (3L1S) model

We further explored the possibility that the anomaly observed near epoch t_1 was caused by a planet orbiting within a binary stellar system. To model this scenario, we employed a triple-lens framework, introducing additional parameters to describe the third (planetary) body. These parameters, (s_3, q_3, ψ) , denote the projected separation and mass ratio of the third body (M_3) relative to the primary lens (M_1), and the orientation angle (ψ) of M_3 measured counterclockwise from the M_1 – M_2 axis. To avoid confusion with the binary-lens parameters, we denote the parameters describing the M_1 – M_2 pair as (s_2, q_2) . A comprehensive summary of the lensing parameters for the various lens-system configurations is provided in Table 2 of C. Han et al. (2023).

The 3L1S modeling was carried out as follows. In the first step, we performed a grid search over the third-body parameters (s_3, q_3, ψ) while fixing all other parameters to those derived from the best-fit 2L1S model. This strategy was motivated by the fact that the 2L1S model adequately reproduces the overall light curve except for the short-term anomaly around t_1 . In the second step, each local solution identified from the grid search was refined by allowing all parameters to vary freely.

The 3L1S modeling yielded two local solutions. The first solution (hereafter A) corresponds to $(s_3, q_3, \psi) \simeq (1.07, 0.49 \times 10^{-3}, 3.59)$, while the second (B) corresponds to $(s_3, q_3, \psi) \simeq (0.39, 12.6 \times 10^{-3}, 0.34)$. In both cases, the small mass ratios indicate that the third body is of planetary mass. The 3L1S model provides a substantially better fit than the 2L2S model, with an improvement of $\Delta\chi^2 = 44.1$, implying that the lens system is a hierarchical triple composed of a planet orbiting a binary stellar host. Figure 5 shows the cumulative distribution of the χ^2 difference, $\Delta\chi^2 = \chi^2_{\text{2L2S}} - \chi^2_{\text{3L1S}}$, between the 2L2S and 3L1S models. The distribution

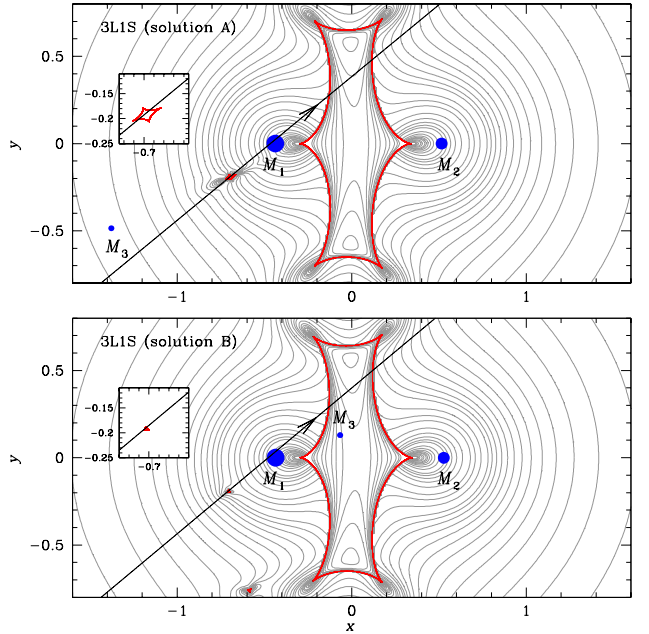


Figure 6. Lens-system configurations for the two 3L1S solutions. The gray curves surrounding the caustics represent contours of equal magnification. The inset in each panel presents a zoomed-in view of the caustic structure generated by the planetary-mass third body (M_3).

shows that the major contribution to $\Delta\chi^2$ arises from the region around t_1 .

The complete sets of lensing parameters for the two 3L1S solutions are listed in Table 1. The corresponding model light curves and residuals around the major anomalies are presented in Figure 4, while the full model light curve for solution A is shown in Figure 1. The two solutions are nearly degenerate, with solution A being slightly preferred by $\Delta\chi^2 = 2.7$. A comparison of the model light curves reveals that solution A features two distinct caustic-crossing spikes, whereas solution B produces a single peak near the caustic exit. This degeneracy could have been resolved if the caustic entrance had been observed. Unfortunately, observations from the KMTC site during the critical epoch of divergence between the two models (HJD' ~ 7511) were lost due to cloudy weather conditions.

Figure 6 displays the lens system configurations for solutions A (upper panel) and B (lower panel). In both cases, the caustic produced by the M_1 – M_2 binary is nearly identical to that of the 2L1S model. The planetary mass third body introduces an additional small caustic, and the source trajectory passes over it, producing the short term anomaly observed around t_1 in the light curve.

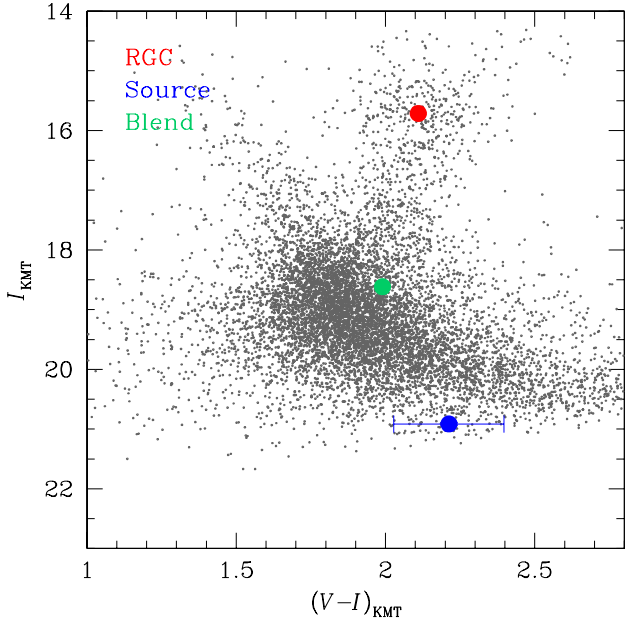


Figure 7. Location of the lensing source in the instrumental color-magnitude diagram. The positions of the red giant clump (RGC) centroid and the blend are also indicated.

Although the two solutions produce similar anomalies, the position of the planet and the structure of the caustic differ between them. In solution A, the planet generates a single four-fold caustic located on the same side as the planet relative to M_1 . Given the relatively wide separation between the planet and the binary, this configuration suggests that the planet is most likely in a circumbinary orbit. In contrast, solution B yields two three-fold caustics situated on the opposite side of M_1 . Because the planet in this case lies at approximately comparable projected separations from both stellar components, it is unlikely to be gravitationally bound to only one star (that is, a circumstellar configuration). Instead, this geometry is more plausibly interpreted as that of a distant planet whose apparent proximity to the binary results from projection effects.

In addition to the geometric differences, the two solutions yield markedly different mass ratios. For solution A, the estimated mass ratio is $q_3 \sim 0.55 \times 10^{-3}$, which is nearly 23 times smaller than that of solution B ($q_3 \sim 12.6 \times 10^{-3}$).

5. ANGULAR EINSTEIN RADIUS

For KMT-2016-BLG-1337, the normalized source radius ρ was measured because the caustic feature at epoch t_3 was well resolved. Combining this measurement with the angular radius of the source star (θ_*) enables the

Table 2. Source parameters, angular Einstein radius, and relative lens-source proper motion.

Parameter	Value
$(V - I, I)$	$(2.213 \pm 0.185, 20.914 \pm 0.025)$
$(V - I, I)_{\text{RGC}}$	$(2.110, 15.714)$
$(V - I, I)_{\text{RGC},0}$	$(1.060, 14.606)$
$(V - I, I)_0$	$(1.163 \pm 0.189, 19.806 \pm 0.032)$
Spectral type	K4V
θ_* (mas)	0.57 ± 0.12
θ_E (mas)	0.53 ± 0.11
μ (mas/yr)	4.73 ± 0.98

determination of the angular Einstein radius as

$$\theta_E = \frac{\theta_*}{\rho}. \quad (1)$$

We estimated the angular source radius by determining its reddening-corrected color and magnitude. To do this, we first derived the instrumental (uncalibrated) source magnitudes in the I and V bands by fitting the observed light curve to the model. The source position was then placed on the instrumental color-magnitude diagram (CMD) for stars lying near the source. In the next step, we calibrated the instrumental source color and magnitude using a reference point on the CMD. Specifically, we adopted the centroid of the red giant clump (RGC) as the reference because its de-reddened color and magnitude are well established from previous studies by [T. Bensby et al. \(2013\)](#) and [D. M. Nataf et al. \(2013\)](#). For both the source flux measurement and the construction of the CMD, we utilized the pyDIA photometry code ([M. Albrow 2017](#)). This code is designed to recover both the differential and reference fluxes from the template image, thereby enabling the reconstruction of the total source flux in instrumental units for each passband.²³

Figure 7 shows the locations of the source and RGC centroid in the instrumental CMD. Using the offsets in color and magnitude, $\Delta(V - I, I)$, between the source and the RGC centroid, $(V - I, I)_{\text{RGC}}$, the de-reddened source color and magnitude, $(V - I, I)_0$, were derived as

$$(V - I, I)_0 = (V - I, I)_{\text{RGC},0} + \Delta(V - I, I), \quad (2)$$

where $(V - I, I)_{\text{RGC},0}$ denote the de-reddened color and magnitude of the RGC centroid. Table 2 lists the cor-

²³ In contrast, the pySIS photometry code, on which the KMTNet photometric pipeline is based, measures only the differential flux with respect to the reference image.

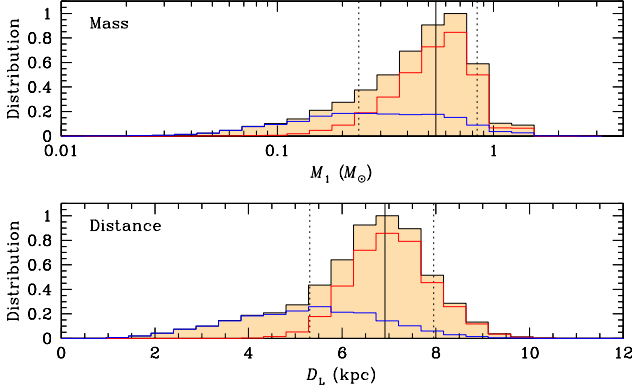


Figure 8. Bayesian posterior distributions for the mass of the primary (heaviest) lens component (M_1) and the distance to the planetary system. In each panel, the blue and red curves represent the contributions from the disk and bulge lens populations, respectively, while the black curve shows the combined posterior distribution. The solid vertical line marks the median value, and the two dotted lines indicate the 1σ confidence interval.

responding values of $(V - I, I)$, $(V - I, I)_{\text{RGC}}$, $(V - I, I)_{\text{RGC,0}}$, and $(V - I, I)_0$. Based on the derived color and magnitude, the source is classified as a mid-K-type main-sequence star located in the Galactic bulge.

Based on the measured source color and magnitude, we derived the angular radius of the source, using the empirical color–surface brightness relation of P. Kervella et al. (2004), which relates $(V - K, V)$ to the stellar angular size. To apply this relation, the observed $(V - I)$ color was converted to $(V - K)$ using the color–color calibration of M. S. Bessell & J. M. Brett (1988). With the resulting estimate of θ_* , we then calculated the angular Einstein radius, θ_E , from Equation (1). Combining θ_E with the measured event timescale, t_E , gives the relative lens–source proper motion, $\mu = \theta_E/t_E$. The derived values of θ_* , θ_E , and μ are summarized in Table 2.

6. NATURE OF THE PLANETARY SYSTEM

We characterize the planetary system by determining the component masses and the distance to the lens. These parameters were derived through a Bayesian analysis of the event. The details of this procedure have been described in numerous previous studies and are not repeated here. In brief, the analysis combines the measured microlensing observables, namely the event timescale (t_E) and the angular Einstein radius (θ_E), with Galactic priors that describe the spatial, kinematic, and mass distributions of potential lenses. A large ensemble of synthetic microlensing events is generated from these priors, and each simulated event is assigned a statistical weight according to its consistency with the

Table 3. Physical parameters of the planetary system.

Parameter	Solution A	Solution B
$M_1 (M_\odot)$	$0.54^{+0.30}_{-0.30}$	←
$M_2 (M_\odot)$	$0.40^{+0.22}_{-0.22}$	$0.44^{+0.24}_{-0.25}$
$M_3 (M_J)$	$0.28^{+0.15}_{-0.16}$	$7.11^{+3.93}_{-3.98}$
$D_L (\text{kpc})$	$6.92^{+1.04}_{-1.61}$	$6.95^{+1.04}_{-1.61}$
$a_{\perp,2} (\text{au})$	$3.54^{+0.53}_{-0.82}$	$3.65^{+0.55}_{-0.85}$
$a_{\perp,3} (\text{au})$	$3.97^{+0.60}_{-0.92}$	$1.49^{+0.22}_{-0.35}$
p_{disk}	34%	←
p_{bulge}	66%	←

measured lensing observables. The resulting weighted ensemble yields posterior probability distributions for the lens mass (M) and distance (D_L). For further details of the analysis procedure, we refer the reader to C. Han et al. (2025a).

Figure 8 presents the posterior distributions for the mass of the most massive lens component, M_1 , and the distance to the lens system derived from the Bayesian analysis. Table 3 summarizes the physical properties of the planetary system, including the individual masses of the lens components (M_1 , M_2 , and M_3), the distance to the system (D_L), and the projected separations of M_2 and M_3 from M_1 ($a_{\perp,2}$ and $a_{\perp,3}$). For each parameter, the reported value corresponds to the median of the posterior distribution, while the lower and upper uncertainties are defined by the 16th and 84th percentiles, respectively. The tables also list the probabilities that the lens resides in the Galactic disk (p_{disk}) or in the bulge (p_{bulge}).

For both solutions, the physical parameters of the host binary stars are essentially identical. The host system comprises two early M-type dwarf stars with masses of approximately $M_1 \sim 0.54 M_\odot$ and $M_2 \sim 0.40 M_\odot$, separated by a projected distance of about $a_{\perp,2} \sim 3.5$ au. The binary system is located at a distance of $D_L \sim 7$ kpc from the Sun in the direction of the Galactic center. The Bayesian analysis further indicates that the system is roughly twice as likely to reside in the Galactic bulge as in the disk.

In contrast, the physical properties of the planet inferred from solutions A and B differ substantially. For solution A, the estimated planet mass is $\sim 0.3 M_J$, comparable to that of Saturn in the Solar System. In solution B, however, the planet is much more massive, with

a derived mass of $\sim 7.1 M_J$. The inferred locations of the planet relative to the host binary stars also differ markedly between the two solutions. As illustrated in Figure 6, in solution A the planet lies on one side of the host binary, whereas in solution B it is positioned between the two stellar components. The projected separations from the primary star are $a_{\perp,3} \sim 4.0$ au for solution A and $a_{\perp,3} \sim 1.5$ au for solution B.

7. SUMMARY AND CONCLUSION

We have analyzed the microlensing event KMT-2016-BLG-1337, which reveals the presence of a planetary companion in a binary system of low-mass stars. The event was observed by the KMTNet survey and independently confirmed by the MOA and OGLE surveys. The light curve exhibits a short-term anomaly superposed on a typical binary-lens profile. Modeling of the event shows that a triple-lens single-source configuration provides the best description, implying that the lens system consists of a planet orbiting a binary stellar host.

The analysis yields two viable solutions that reproduce the observed anomaly equally well. In solution A, the planet has a mass of $M_3 \sim 0.3 M_J$ at a projected separation of $a_{\perp,3} \sim 4$ au, while in solution B, the planet is more massive ($M_3 \sim 7 M_J$) and located closer to the host stars ($a_{\perp,3} \sim 1.5$ au). Although the two models differ in their interpretation of the planetary anomaly, the available data do not allow the degeneracy to be conclusively resolved, primarily due to missing coverage during the caustic entrance phase. A Bayesian analysis based on Galactic priors indicates that the host sys-

tem is composed of two early M-dwarf stars with masses of $M_1 \sim 0.54 M_{\odot}$ and $M_2 \sim 0.40 M_{\odot}$, separated by $a_{\perp,2} \sim 3.5$ au and located at $D_L \sim 7$ kpc toward the Galactic bulge.

The event KMT-2016-BLG-1337L underscores the capability of microlensing to reveal planets in dynamically complex stellar environments, including systems that are inaccessible to conventional detection techniques. This expands the census of planets in multiple-star systems and contributes to a more comprehensive understanding of planet formation in such environments.

ACKNOWLEDGEMENTS

C.H. was supported by the Chungbuk National University 2025 NUDP program and the National Research Foundation of Korea (RS-2025-21073000). This research has made use of the KMTNet system operated by the Korea Astronomy and Space Science Institute (KASI) at three host sites of CTIO in Chile, SAAO in South Africa, and SSO in Australia. Data transfer from the host site to KASI was supported by the Korea Research Environment Open NETwork (KREONET). The OGLE project has received funding from the Polish National Science Centre grant OPUS-28 2024/55/B/ST9/00447 to AU. H.Y. and W.Z. acknowledge support by the National Natural Science Foundation of China (Grant No. 12133005). The MOA project is supported by JSPS KAKENHI Grant Number JP16H06287, JP22H00153 and 23KK0060. C.R. was supported by the Research fellowship of the Alexander von Humboldt Foundation.

REFERENCES

- Alard, C.; Lupton, R. H. 1998, ApJ, 503, 325, doi: [10.1086/305984](https://doi.org/10.1086/305984)
- Albrow, M. 2017, MichaelDAlbrow/pyDIA: Initial Release on Github, Versionv1.0.0, Zenodo, doi: [10.5281/zenodo.268049](https://doi.org/10.5281/zenodo.268049)
- Albrow, M. D., Horne, K., Bramich, D. M., et al. 2009, MNRAS, 397, 2009, doi: [10.1111/j.1365-2966.2009.15098.x](https://doi.org/10.1111/j.1365-2966.2009.15098.x)
- Bennett, D. P., Rhie, S. H., Udalski, A., et al. 2016, AJ, 152, 125, doi: [10.3847/0004-6256/152/5/125](https://doi.org/10.3847/0004-6256/152/5/125)
- Bennett, D. P., Udalski, A., Bond, I. A., et al. 2020, AJ, 160, 72, doi: [10.3847/1538-3881/ab9cb9](https://doi.org/10.3847/1538-3881/ab9cb9)
- Bensby, T., Yee, J. C., Feltzing, S., et al. 2013, A&A, 549, A247, doi: [10.1051/0004-6361/201220678](https://doi.org/10.1051/0004-6361/201220678)
- Bessell, M. S., & Brett, J. M. 1988, PASP, 100, 1134, doi: [10.1086/132281](https://doi.org/10.1086/132281)
- Bond, I. A., Abe, F., Dodd, R. J., et al. 2001, MNRAS, 327, 868, doi: [10.1046/j.1365-8711.2001.04776.x](https://doi.org/10.1046/j.1365-8711.2001.04776.x)
- Gould, A., Udalski, A., Shin, I.-G., et al. 2014, Science, 345, 46, doi: [10.1126/science.1251527](https://doi.org/10.1126/science.1251527)
- Han, C., Lee, C.-U., Udalski, A., et al. 2025a, A&A, 699, A91, doi: [10.1051/0004-6361/202554182](https://doi.org/10.1051/0004-6361/202554182)
- Han, C., Lee, C.-U., Udalski, A., et al. 2020, AJ, 159, 48, doi: [10.3847/1538-3881/ab5db9](https://doi.org/10.3847/1538-3881/ab5db9)
- Han, C., Shin, I.-G., & Jung, Y. K. 2017a, ApJ, 835, 115, doi: [10.3847/1538-4357/835/2/115](https://doi.org/10.3847/1538-4357/835/2/115)
- Han, C., Udalski, A., Jung, Y. K., et al. 2024, A&A, 685, A16, doi: [10.1051/0004-6361/202348791](https://doi.org/10.1051/0004-6361/202348791)
- Han, C., Udalski, A., Jung, Y. K., et al. 2023, A&A, 670, A172, doi: [10.1051/0004-6361/202245525](https://doi.org/10.1051/0004-6361/202245525)
- Han, C., Udalski, A., Kim, D., et al. 2021, AJ, 161, 270, doi: [10.3847/1538-3881/abf4d0](https://doi.org/10.3847/1538-3881/abf4d0)

- Han, C., Udalski, A., Lee, C.-U., et al. 2025b, A&A, 700, A181, doi: [10.1051/0004-6361/202452760](https://doi.org/10.1051/0004-6361/202452760)
- Han, C., Udalski, A., Gould, A., et al. 2017b, AJ, 154, 223, doi: [10.3847/1538-3881/aa9179](https://doi.org/10.3847/1538-3881/aa9179)
- Kervella, P., Thévenin, F., Di Folco, E., & Ségransan, D. 2004, A&A, 426, 297, doi: [10.1051/0004-6361:20035930](https://doi.org/10.1051/0004-6361:20035930)
- Kim, D.-J., Kim, H.-W., Hwang, K.-H., et al. 2018, AJ, 155, 76, doi: [10.3847/1538-3881/aaa47b](https://doi.org/10.3847/1538-3881/aaa47b)
- Kim, S.-L., Lee, C.-U. and Park, B.-G., Kim, D.-J., et al. 2016, JKAS, 49, 37, doi: [10.5303/JKAS.2016.49.1.37](https://doi.org/10.5303/JKAS.2016.49.1.37)
- Lee, D.-W., Lee, C.-U., Park, B.-G., et al. 2008, ApJ, 672, 623, doi: [10.1086/523662](https://doi.org/10.1086/523662)
- Nataf, D. M., Gould, A., Fouqué, P., et al. 2013, ApJ, 769, 88, doi: [10.1088/0004-637X/769/2/88](https://doi.org/10.1088/0004-637X/769/2/88)
- Poleski, R., Skowron, J., Udalski, A., et al. 2014, ApJ, 795, 42, doi: [10.1088/0004-637X/795/1/42](https://doi.org/10.1088/0004-637X/795/1/42)
- Sumi, T., Abe, F., Bond, I. A., et al. 2003, ApJ, 591, 204, doi: [10.1086/375212](https://doi.org/10.1086/375212)
- Tomaney, A. B., & Croots, A. P. S. 1996, AJ, 112, 2872, doi: [10.1086/118228](https://doi.org/10.1086/118228)
- Udalski, A. 2003, Acta Astron., 53, 291, doi: [10.48550/arXiv.astro-ph/0401123](https://doi.org/10.48550/arXiv.astro-ph/0401123)
- Udalski, A., Szymański, M. K., & Szymański, G. 2015, Acta Astron., 65, 1, doi: [10.48550/arXiv.1504.05966](https://doi.org/10.48550/arXiv.1504.05966)
- Wozniak, P. R. 2000, Acta Astronomica, 50, 421, doi: [10.48550/arXiv.astro-ph/0012143](https://doi.org/10.48550/arXiv.astro-ph/0012143)
- Yang, H., Yee, J. C., Hwang, K.-H., et al. 2025, MNRAS, 528, 11, doi: [10.1093/mnras/stad3672](https://doi.org/10.1093/mnras/stad3672)
- Zang, W., Han, C., Kondo, I., et al. 2021a, Research in Astronomy and Astrophysics, 21, 239, doi: [10.1088/1674-4527/21/9/239](https://doi.org/10.1088/1674-4527/21/9/239)
- Zang, W., Hwang, K.-H., Udalski, A., et al. 2021b, AJ, 162, 163, doi: [10.3847/1538-3881/ac12d4](https://doi.org/10.3847/1538-3881/ac12d4)